Development and Performance Validation of an Infrared-Hot Air Combined Drying Test Bench for a Thin Layer of Rice

Chunshan Liu,[a] Xiaowei Gao,[a] Siyu Chen,[b,*] Anran Wang,[a] Kezhen Chang,[a] Jingjing Kong,[a] Zhengyu An,[a] and Jie Li [a]

To enhance the uniformity and efficiency of rice drying, an infrared hot air combined drying test bench was developed, and the air flow distribution inside the pipeline was optimized to achieve efficient and uniform drying. The pipeline structure was optimized by using computational fluid dynamics simulation technology, with relative standard deviation (CV) and uniformity index (UI) as evaluation indicators. The airflow uniformity of the optimized pipeline and the temperature uniformity of the drying chamber were verified through experiments. The numerical simulation results showed that after the structural optimization, the UI of the pipeline outlet was increased from 92.27% to 97.23%, and the CV was decreased from 22.34% to 14.62%. Experimental verification shows that the wind speed uniformity index of the optimized pipe section is 97.67%, which is in good agreement with the simulated value (the relative error of the average speed is 1.50%), and the temperature change in the drying chamber is stable within ±2.5%. Further drying performance tests were conducted on two types of rice. Under the conditions of a hot air temperature of 45℃, a wind speed of 3 m/s, and a thin layer thickness of 20 mm, the performance of infrared hot air combined drying and hot air drying was compared. The performance test results show that the infrared hot air combined drying only takes 120 minutes, which is 18.75% shorter than the single hot air drying time, and still maintains a relatively high drying rate during the deceleration and dehydration stage. Improving the uniformity of air flow distribution can significantly enhance the uniformity of drying. Infrared hot air combined drying has good application potential in terms of improving efficiency and energy conservation.

DOI: 10.15376/biores.21.1.2330-2350

Keywords: Infrared and hot air combined drying; Structural optimization; Numerical simulation; Rice drying

*Contact information: a: College of Mechanical Engineering Jiamusi University, Jiamusi 154007, China; b: College of Mechanical and Automotive Engineering Bengbu University, Bengbu 233030, China; *Corresponding author: chensiyu516@163.com*

INTRODUCTION

Since the implementation of the 14th Five-Year Plan, China's annual rice output has consistently surpassed 200 million metric tons. This sustained production level plays a critical role in safeguarding national food security and supporting steady economic development (Chen *et al.* 2024; Liu *et al.* 2024).

In the agricultural sector, the post-harvest drying process of grains consumes a high proportion of energy and has a low utilization efficiency. Its energy consumption accounts for approximately 10% to 15% of the total industrial energy consumption, while the

efficiency is only 10% to 20% (Hu 2006). To address this challenge, the adoption of multi-coupling drying technology - that is, combining different drying methods in parallel or series - has become an important research direction for improving the drying efficiency of high-moisture grains and reducing energy consumption.

In recent years, infrared-hot air combined drying technology has matured significantly and been widely applied in drying research for various materials (Chen *et al.* 2024; Dai *et al.* 2024). Infrared radiation and hot air synergistic drying: Infrared radiation penetrates the interior of the material in the form of electromagnetic waves, directly heating water molecules to generate bulk heat, driving the internal moisture to migrate outward. The hot air, on the other hand, efficiently removes the vaporized moisture from the surface of the material through convection and continuously supplies hot air. The combination of the two not only overcomes the shortcoming of slow surface moisture discharge in single infrared drying, but also solves the efficiency bottleneck caused by external overheating and slow internal heat transfer in single hot air drying, thereby greatly improving the drying efficiency and reducing energy consumption. (Geng *et al.* 2024; Nuthong *et al.* 2024; Wang *et al.* 2024). Wu *et al.* (2020) found through experiments that infrared-hot air combined drying reduced drying time by 16.7% compared to hot air drying alone. Other researchers (Dai *et al.* 2013) have investigated the interaction factors and optimized process parameters for combined infrared and convective drying. Jeevarathinam (2025), studying ginger slice drying, observed that the majority of moisture evaporation in Sichuan pepper occurs during the falling rate period. Xue *et al.* (2023), investigated a thin-layer far-infrared hot air combined drying of Sichuan pepper and designed a tray-type combined hot air and infrared dryer to analyze changes in material color and moisture content during drying. Zhang *et al.* (2019) demonstrated that infrared-assisted hot air drying better preserves curcumin, oils, and starch in turmeric. However, in the different drying stages of the combined drying process, the primary and secondary influencing factors of the two heat sources on the precipitation rate remain unclear. This paper studied the drying characteristic curves of short-grain Hongfa 17 japonica rice and long-grain Longqing 12 japonica rice to explore how the correct matching of infrared and hot air is more conducive to the drying efficiency of rice.

Rice, as a heat-sensitive material, requires precise control during its drying process. If the drying is insufficient, the moisture content of the grains will be too high, and they are very likely to mold during storage. This not only leads to the loss of nutrients but also breeds harmful substances such as aflatoxin, posing a food safety risk. Conversely, if the rice is overly dried, the intense thermal effect and moisture gradient will cause the grains to crack or even burst, directly leading to a decrease in the proportion of whole polished rice, damaging the edible quality of the rice, and thus seriously damaging its nutritional and economic value.

Drying uniformity is a key performance indicator for drying equipment and processes. Improving airflow distribution can effectively enhance the drying characteristics of materials. Numerous studies (Li *et al.* 2013; Cui *et al.* 2015) have focused on structural optimization of airflow distribution, primarily targeting the air distribution chamber as a critical component. Jiang *et al.* (2022) optimized the air distribution chamber using computational fluid dynamics (CFD) simulations, achieving air velocity and temperature deviations within ±3%. Dai *et al.* (2013) conducted numerical simulations on the chamber of a gas-jet dryer, employing a flat-plate spoiler model to address airflow non-uniformity. Li *et al.* (2018) identified the cavity thickness of the distribution chamber as a key factor influencing airflow uniformity.

To mitigate the impact of vortices on flow field uniformity caused by 90-degree bends, a gradually converging pipe (tapered tube) design was adopted for optimization. Liu *et al.* (2005) performed finite element analysis on the transition section of tapered tubes, finding that the diameter transition ratio (transition arc radius) significantly affects flow rate. Cui *et al.* (2015) simulated flow patterns in straight and tapered pipes using CFD, demonstrating that tapered tubes exhibit a more pronounced entrainment effect than straight pipes.

To explore the drying characteristics of rice under the combined effect of infrared radiation and hot air and the primary and secondary influencing factors, considering the experimental requirements such as temperature and wind speed uniformity, an infrared hot air combined drying device was designed, and the problem of uneven air flow was solved to improve the drying uniformity. This study aims to address the issue of uniform heating and drying of materials within the drying oven by optimizing the airflow distribution in the upstream pipeline. For the problem of curve diversion, the ventilation duct of the test bench was optimized by gradually reducing the diameter of the duct. The optimization parameters of the duct were determined through numerical calculation simulation, and experiments were carried out to verify the uniformity of the air velocity at the air inlet of the drying chamber and the uniformity of the temperature inside the drying chamber. Short-grain Hongfa 17 japonica rice and long-grain Longqing 12 japonica rice of different shapes were selected as the test objects. The rice was laid flat on a screen with a thickness of 20 mm, and three-layer 20 mm hot air drying and single-layer 20 mm infrared hot air combined drying experiments were conducted respectively to verify the performance of the entire machine.

EXPERIMENTAL

Overall Structure

The structural schematic diagram of the infrared hot air combined drying test bench is shown in Fig. 1, and it includes four parts: the infrared hot air combined drying module, the automatic weighing module, the material support system and the information collection module.

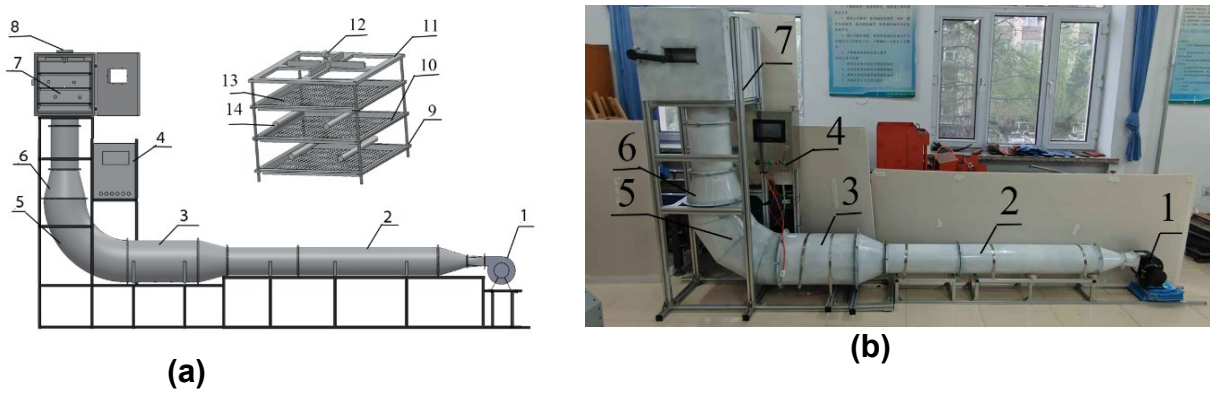

Fig. 1. (a) Diagram of infrared combined hot air drying test platform and (b) photo of infrared and thermal convection combined drying device. 1. centrifugal fan, 2. uniform air pipe, 3. heating pipe, 4. control box 5. 90° curve 6. shrinking tube 7. drying box 8. exhaust valve 9. screw rod 10. material pallet support 11. fixed support 12. lifting eye 13. infrared radiation heating pipe 14. material tray

Working Principle

The screened rice samples were evenly spread on the material trays. The rice was dried through the combined action of far-infrared radiation emitted by carbon fiber infrared heating tubes positioned above the trays and hot air supplied from the bottom of the drying chamber. Heat was transferred to the rice grains *via* thermal conduction from both the infrared radiation and the hot air. This drives internal moisture diffusion towards the grain surface. Simultaneously, surface moisture was heated and vaporized into water vapor, which was then removed from the drying chamber by the airflow. An acquisition module collected data *via* sensors, including infrared heating tube temperature, thin-layer rice temperature, drying chamber air velocity, and humidity. This data was transmitted to a PLC (Programmable Logic Controller). The PLC employed a PID (Proportional-Integral-Derivative) control algorithm to regulate the power supplied to both the electric heating elements (for hot air generation) and the carbon fiber infrared heating tubes. The acquired data were also sent to an HMI (Human-Machine Interface) for real-time display and monitoring. An automatic weighing module continuously monitored the weight change of the samples during drying, providing an indirect determination of material moisture content. When the load cell detected that the weight had reached the pre-set termination value, the PLC automatically deactivated the infrared heating tubes and the air blower, stopping the drying process.

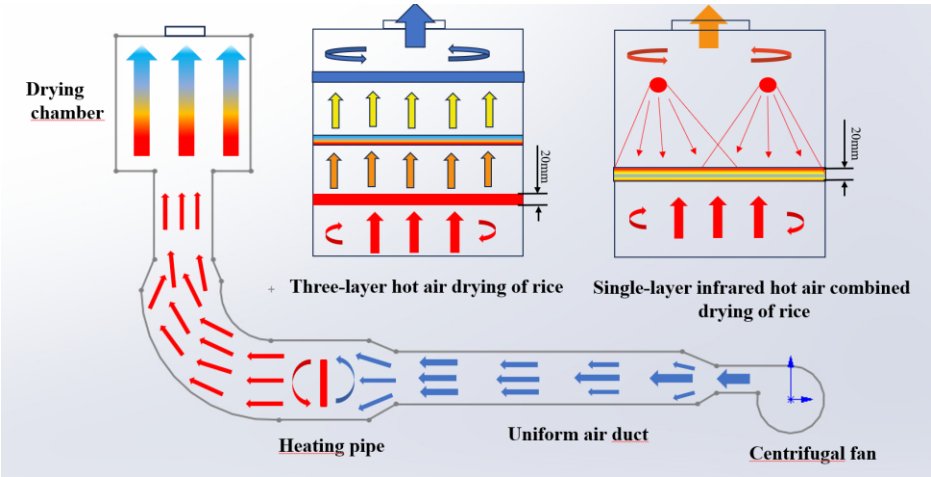

Fig. 2. Schematic diagram of the working principle of the test bench

Pipeline Design Optimization and Numerical Simulation

The CFD simulation of this stage aimed to optimize the air supply duct in front of the drying oven to ensure that the airflow entering the drying oven was uniform. A further goal was to solve the problem of uniform heating of the thin layer of rice inside the drying oven. The simulation at this time did not include the rice bed layer. A large number of studies have shown that the air distribution chamber is a key component of hot air drying equipment and also the primary factor to be considered when designing new types of dryers. Different design methods should be adopted for different dryer structures to conduct relevant structural and technical parameter research.

The three fundamental equations of fluid mechanics are the energy conservation equation, the momentum conservation equation, and the continuity equation. Given that the Reynolds number exceeded 2300, a turbulent flow model was selected for simulation.

Among the commonly used turbulence models in Fluent simulations are the Standard k-ε model, RNG k-ε model, Realizable k-ε model, and the k-ω model. The Realizable k-ε model was chosen for this study due to its ability to ensure reliable accuracy within the core turbulent flow region of pipes and provide reasonably accurate predictions of pressure loss, mean velocity distribution, and overall flow characteristics. The governing equations for the adopted Realizable k-ε turbulence model are listed below.

Continuity equation:

$$\nabla \cdot u = 0 \tag{1}$$

Momentum Equation:

$$\frac{\partial u}{\partial t} + u \cdot \nabla u = -\rho \nabla p + \mu \nabla^2 u \tag{2}$$

Turbulence model equation (k-equation):

$$\frac{\partial}{\partial t}(\rho k) + \nabla(\rho \mathbf{u} k) = \nabla(\Gamma_k \nabla k) + G_k - Y_k \tag{3}$$

Turbulence Model Equations (ε Equations):

$$\frac{\partial}{\partial t}(\rho \varepsilon) + \nabla(\rho \mathbf{u} \varepsilon) = \nabla(\Gamma_\varepsilon \nabla_\varepsilon) + G_\varepsilon - Y_\varepsilon \tag{4}$$

In these equations, u is the fluid velocity vector (m/s), ρ is the fluid density (kg/m³), p is the static pressure (Pa), μ is the effective dynamic viscosity (Pa·s), k is the turbulent kinetic energy (m²/s²), Γ_k is the effective diffusivity for k, G_k is the generation term of turbulent kinetic energy, Y_k is the dissipation term of turbulent kinetic energy, ε is the turbulent dissipation rate (m²/s³), Γ_ε is the effective diffusivity for ε, G_ε is the generation term of ε, and Y_ε is the dissipation term of ε.

Boundary Conditions

The fluid medium within the pipe was air, modeled as an incompressible fluid. The inlet of the bent pipe was defined as a velocity inlet boundary condition, with an inlet air velocity set to 5 m/s. The backflow turbulent intensity was specified as 3.78%, and the hydraulic diameter was 0.3 m. The outlet of the bend was defined as a pressure outlet boundary condition, with the gauge pressure set to 0 Pa. Suppose the pipe wall is defined as an adiabatic non-slip wall boundary. The solver was set to the discrete format of the second-order upwind format, and the simple algorithm based on the pressure-velocity coupling was applied. The residual accuracy was set to 10^{-4} for numerical simulation. The turbulence calculation adopts the k-epsilon equation model of the standard wall, which closes the Reynolds mean N-S equation system by solving the turbulent kinetic energy and its dissipation rate transport equation. The turbulent intensity was calculated using the following formula:

$$I = 0.16(Re)^{-0.125} \tag{5}$$

where I is the reflux turbulence intensity, and Re is the Reynolds number.

Grid Independence Verification

To determine the appropriate number of grids, the variation of the average velocity of the pipe outlet section under different grid numbers was monitored, and grid independence verification was conducted. The results are shown in Fig. 2. This paper analyzed the variation law of the velocity field parameters of the characteristic section at the exit of a curve with grid densification by constructing eight different scales of grid numbers (175,700, 359,700, 520,900, 793,500, 1,090,500, 1,290,400, 1,530,600, and 1,652,200). Based on a comprehensive consideration of calculation accuracy and efficiency, the minimum grid size was set at 0.5 mm and the maximum at 4 mm. The total number of grids was approximately 1.0905 million.

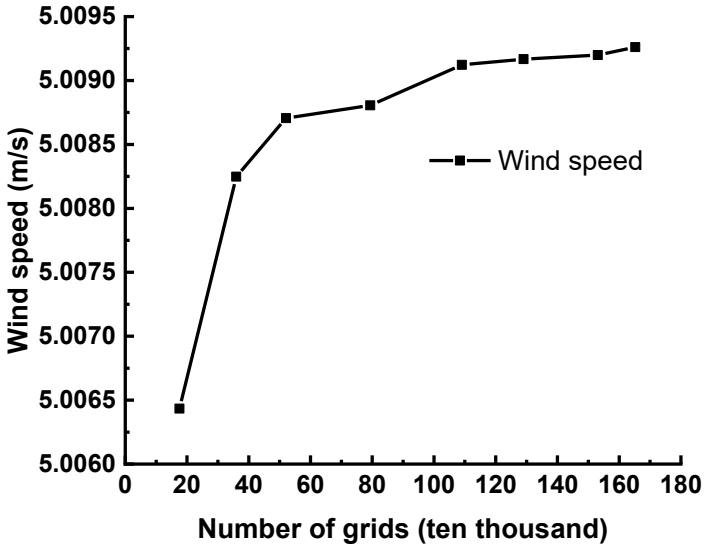

Fig. 3. Grid independence verification

Evaluation Indicators

The coefficient of variation (CV) and the uniformity index (UI) were employed to analyze the air velocity uniformity at the pipe outlet cross-section.

The UI serves as an evaluation criterion for quantifying the velocity uniformity within a flow field. This metric provides a precise characterization of the uniformity characteristics in the fluid velocity distribution across the flow cross-section. Furthermore, it demonstrates good comparability across varying operating conditions (Li *et al.* 2013). The UI was calculated as follows,

$$\gamma_v = 1 - \frac{1}{2n} \sum_{j=1}^{n} \frac{\sqrt{\left(v_j - \overline{v}\right)^2}}{\overline{v}} \tag{6}$$

where γ_v is the uniformity index, which takes the value [0,1]. The higher the value, the better the flow uniformity. The variable v_j is the velocity of the velocity measurement point and $\overline{v}$ is the uniform velocity of the measurement plane, unit: m/s, $\overline{v}$ is the average velocity, unit: m/s.

The CV quantifies the degree of dispersion around the mean value, while serving as a quantitative indicator for comparing enhancement levels in flow field uniformity (Tao *et al.* 2010; Fan *et al.* 2020). The CV was calculated as follows,

$$CV = S / \bar{v} \tag{7}$$

$$S = \sqrt{\frac{1}{n-1}\sum_{j=1}^{n}\left(v_j - \bar{v}\right)^2} \tag{8}$$

where CV is the relative standard deviation, S is the standard deviation, and $\bar{v}$ is the average velocity.

Pipeline Structure Optimization

Flow field analysis of the original structure

As shown in Fig. 4, under the effect of the 90° bend, the airflow direction underwent a drastic change, generating obvious wall separation on the inner side of the pipe and forming vortices, which intensified the stability of the flow velocity at the outlet section. There was a significant difference in wind speed between the inner and outer sides of the outlet section, with a relative standard deviation of 22.34% and a homogeneity index of 92.27%. The airflow on the outer side showed a wall-hugging movement, while there was a distinct diversion on the inner side of the curve. When the fluid passed through the curve, the fluid pressure on the outer side of the curve pipe increased due to the effect of centrifugal force. This unevenly distributed pressure caused the fluid to shift (Liu *et al.* 2005).

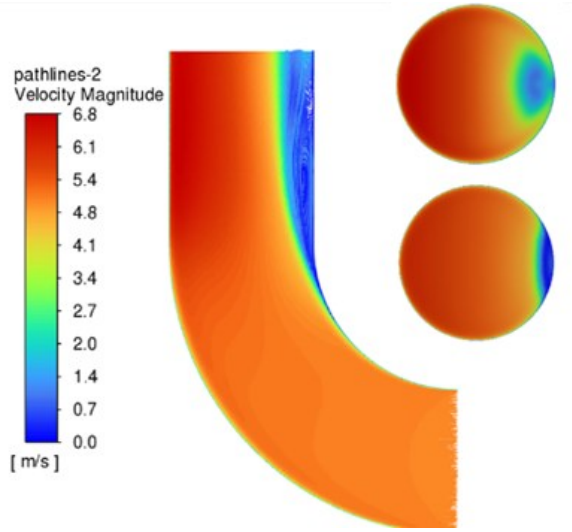

Fig. 4. Original pipeline flow velocity trajectory diagram

Optimized Post-structural Analysis

To mitigate the non-uniform flow distribution induced by pipe bends, a gradually converging section (tapered pipe) was implemented. This design enhances outlet air velocity and increases inertial effects, thereby suppressing local flow disturbances. However, excessive flow velocity must be avoided to minimize energy losses associated with elevated frictional resistance. The flow characteristics within tapered pipes are primarily governed by the diameter ratio (A_1/A_2), contraction length (H), and transition

geometry (Fan 2020). Research by Fan (2020) demonstrates that the optimal contraction angle for a straight-to-tapered pipe transition is 60°. At this angle, fluctuations in inlet velocity within the design range exhibit negligible impact on the local loss coefficient. Therefore, numerical simulations were conducted to evaluate flow uniformity at the outlet cross-section. This assessment utilized the coefficient of variation (CV) and uniformity index (UI) across varying contraction lengths (H) (50, 100, 125, 150, 175, 200, or 250 mm) and diameter ratios (A_1/A_2) (1.2, 1.5, or 2.0). A schematic diagram of the tapered pipe configuration is shown in Fig. 5.

Fig. 5. Schematic diagram of tapered duct structure and computational mesh generation. (a) Pipe dimension drawing, (b) model meshing diagram

Velocity and pressure contours (Fig. 6) for the tapered pipe configuration with a contraction length (H) of 200 mm and a diameter ratio (A_1/A_2) of 1.5 demonstrated that the gradual contraction positively influences the hydrodynamic characteristics. It effectively mitigates flow separation and vortex formation, thereby enhancing flow uniformity. At the pipe outlet, the mean air velocity reached 11.26 m/s, with a uniformity index (UI) of 97.23% and a coefficient of variation (CV) of 14.62%. These metrics indicate significantly improved uniformity in both velocity and pressure distribution at the outlet.

Fluid passing through the 90° bend exhibited relatively minor fluctuations in velocity and static pressure, maintaining stable flow conditions. However, upon entering the tapered section, the velocity displayed a distinct vertical gradient increase, while static pressure demonstrated a graded decrease. This pressure-velocity trade-off resulted in localized energy losses, primarily governed by the transition profile geometry. At the tapered section outlet, velocity peaked at 12.9 m/s and static pressure dropped to its minimum of -30.1 Pa, highlighting the section's pronounced effect on modulating fluid kinetic and pressure energy. Subsequently, as flow progressed through the straight pipe section, velocity stabilized while static pressure gradually recovered, increasing to 1.9 Pa.

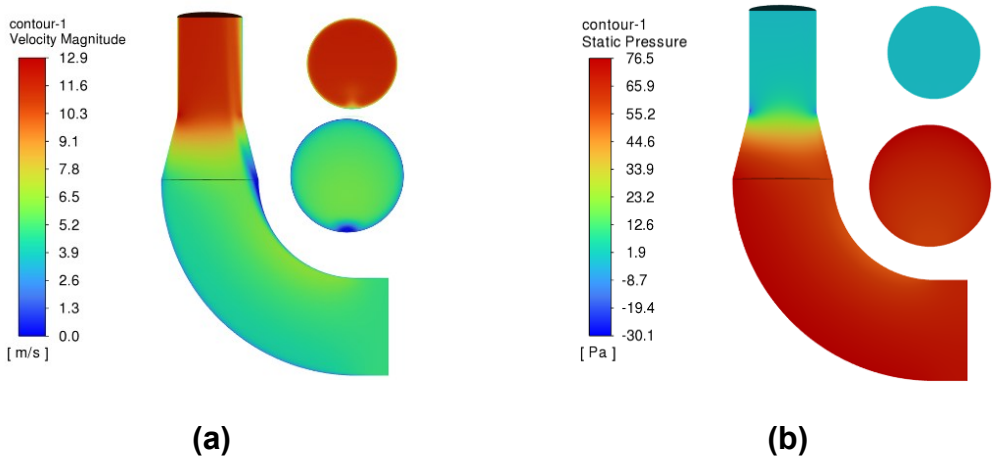

Fig. 6. Optimized tapering pipe (a) velocity contour and (b) pressure contour

Relationship Between Diameter Ratio and Outlet Flow Uniformity

At a constant inlet velocity of 5 m/s, the configuration with a diameter ratio (A_1/A_2) of 1.5 demonstrated superior flow uniformity at the pipe outlet compared to a ratio of 1.2. The Uniformity Index (UI) exhibited a marked increasing trend with contraction length (H) over the 50 to 250 mm range, rising from an initial value of 95.90% to 97.33%. Concurrently, the Coefficient of Variation (CV) decreased proportionally, forming mutually reinforcing data trends.

For an diameter ratio of 1.2, the UI remained within a tight range of 96.0% ± 0. 3%. Between 150 and 250 mm, the UI profile approached horizontal asymptote behavior, indicating minimal sensitivity to contraction length variation. At a diameter ratio of 2.0, the CV stabilized within the 150 and 250 mm contraction length range. However, this configuration yielded an outlet velocity of 20.03 m/s, resulting in thermal focusing at the center of the rice thin-layer. Consequently, this design is less suitable for uniform drying applications.

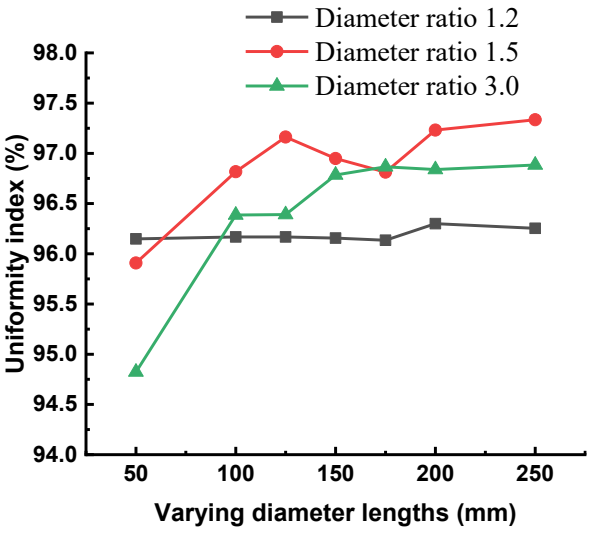

Fig. 7. Uniformity index of a converging duct under varying transition lengths

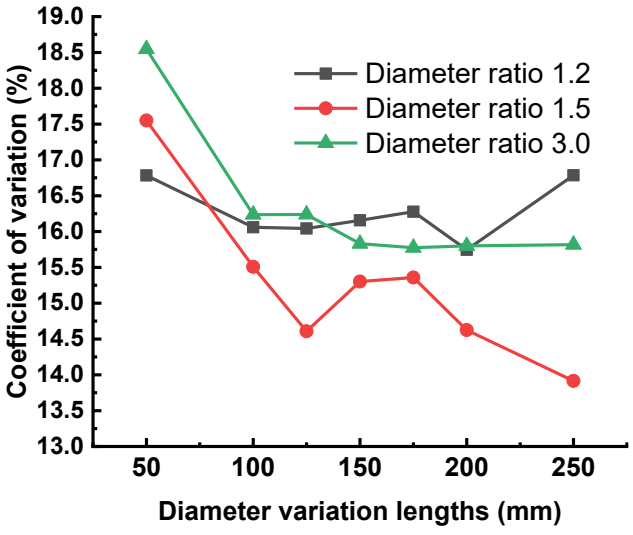

Fig. 8. Relative standard deviation of a converging duct under varying transition lengths

Relationship Between Contraction Length and Outlet Flow Uniformity

The velocity cloud diagrams of different tapering lengths with a diameter ratio of 1.5 are shown in Fig. 9. After installing the tapering pipe at the 90° elbow outlet, the fluid momentum at the pipe outlet was increased, significantly improving the uniformity of the flow velocity at the outlet section.

As the length of the diameter change increased, the flow of the fluid in the pipeline became more stable. The flow velocity gradient through the tapered tube was wider, which caused the maximum flow velocity at the outlet boundary of the tapered tube to continuously decrease, from the maximum flow velocity of 17.8 m/s with a diameter change length of 50 mm to 12.9 m/s.

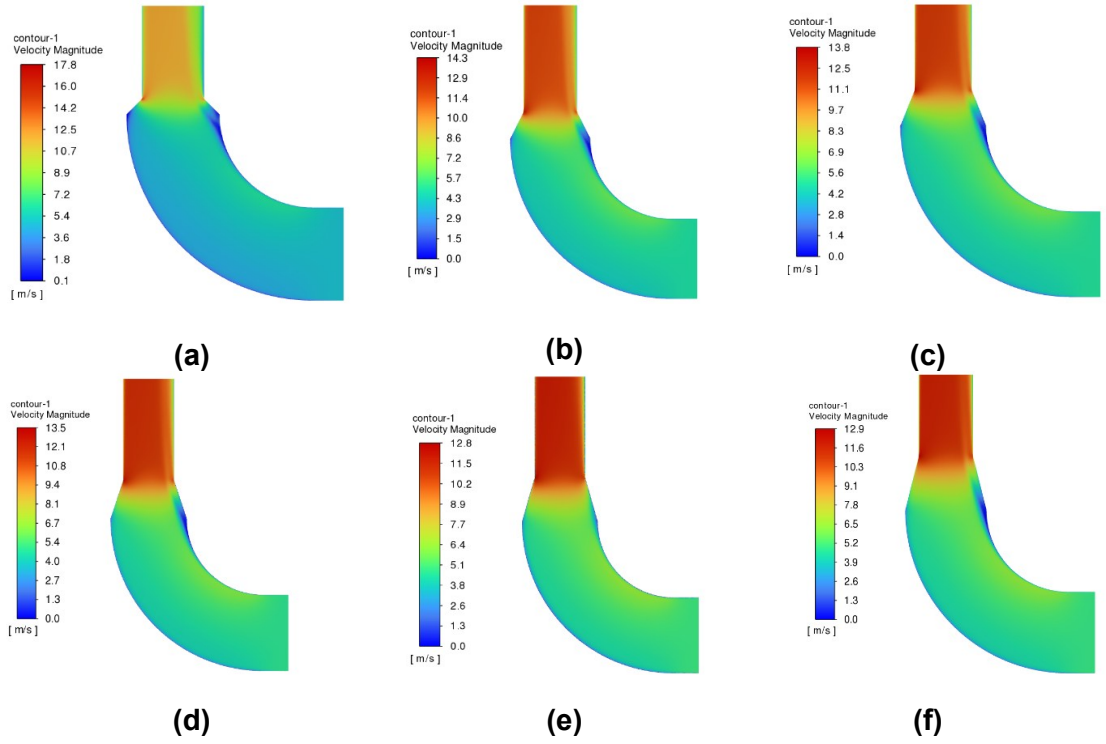

Fig. 9. Velocity contours of a converging duct with a diameter ratio of 1.5 under varying transition lengths of (a) 50, (b) 100, (c) 120, (d) 150, (e) 175, or (f) 200 mm

Experimental Verification Analysis

Pipeline wind speed unevenness analysis

To validate the effectiveness of the duct structural optimization, experimental verification of air velocity uniformity was conducted at the outlet cross-section. Sampling point locations and quantities followed the specifications for circular ducts in GB/T 50243-2016 (Code for Acceptance of Construction Quality of Ventilation and Air Conditioning Works).

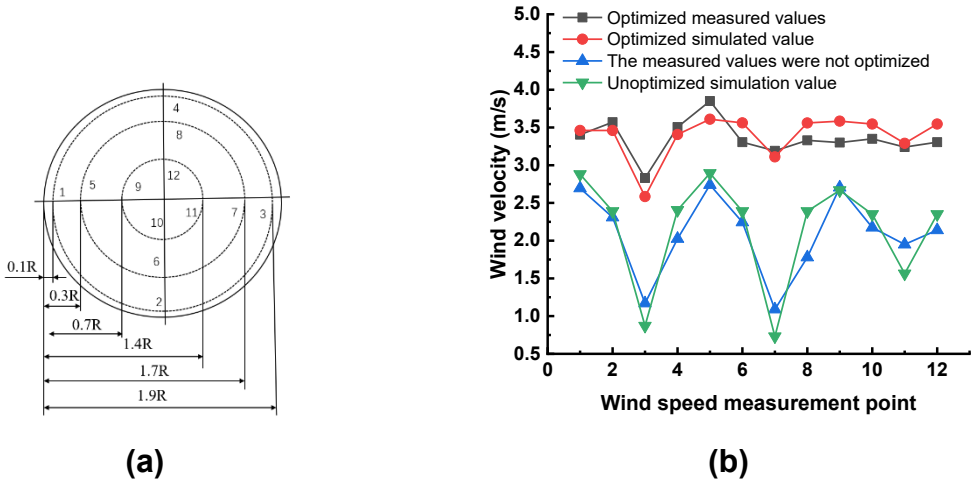

Fig. 10. (a) Diagram of wind speed measurement points selection; (b) comparison of simulated *vs*. measured air outlet wind speed

The measurement protocol involved dividing the duct cross-section into an appropriate number of concentric annuli. Next, measurement points were positioned at the intersections of each annulus's centerline with two perpendicular diameters, where *R* represents the duct radius at the measurement cross-section. Twelve measurement points were established at the normalized radial positions of 0.1R, 0.3R, 0.6R, 1.4R, 1.7R, and 1.9R.

As shown in Fig. 10, by gradually reducing the diameter to optimize the pipeline, the air velocity at the outlet was increased and mainly maintained at around 3.5 m/s, meeting the air velocity requirements of the device (1 m/s to 3 m/s). Among them, the measured cross-sectional wind speed uniformity index after optimization was 97.67%, and the measured cross-sectional wind speed uniformity index of the original pipeline was 89.87%. Due to the unstable instantaneous airflow velocity at some individual positions, there was a deviation between the measured values and the simulated values at the corresponding points. However, the overall cross-sectional wind speed distribution trend was consistent. Through data analysis, it can be known that the relative error of the average speed between the optimized measured value and the simulated value was 1.50%, the relative error of the speed uniformity index was 6.23%, and the relative error of the speed relative standard deviation was 7.4%. The simulation data was in good agreement with the measured data, verifying the accuracy of the model.

Temperature Uniformity Analysis of the Drying Chamber

To ensure uniform drying performance of the apparatus, temperature uniformity tests were conducted in accordance with GB/T 30435-2013 (Electrically heated drying ovens and blast drying ovens). Designated measurement points (Fig. 10) were monitored at three temperatures: 30, 50, and 70 °C. Following thermal equilibrium maintenance (2 h stabilization), temperatures were recorded at 1-min intervals across all points for 30 min.

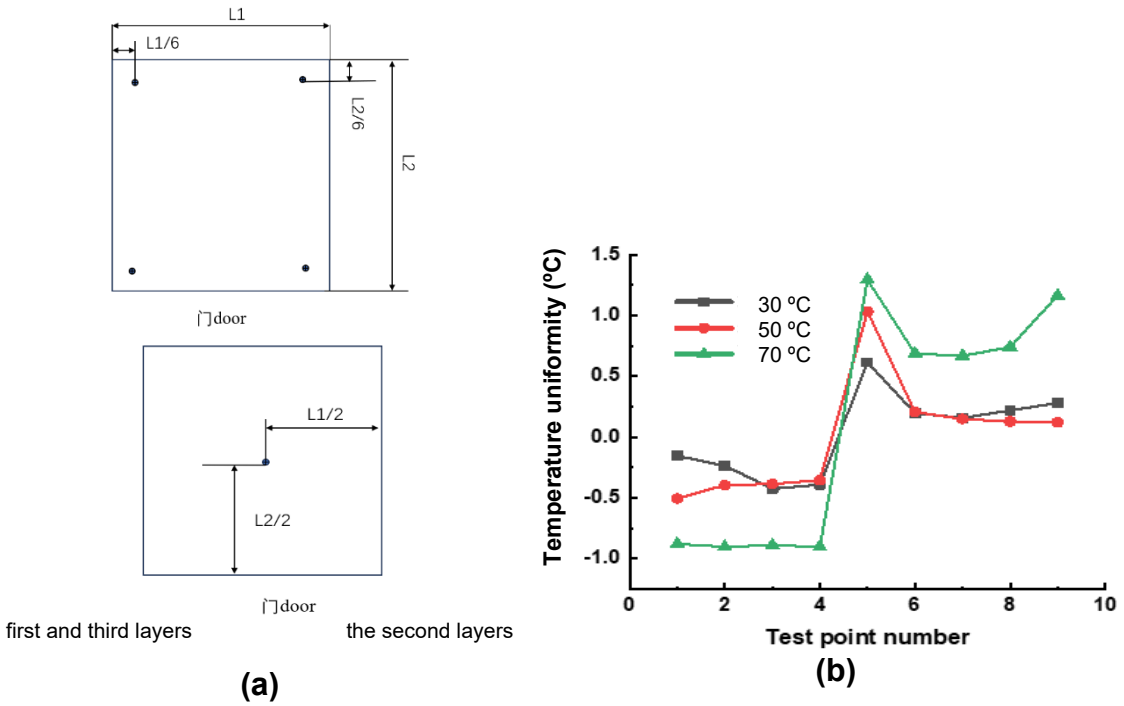

Fig. 11. (a) Diagram of air temperature measurement points and (b) internal temperature uniformity diagram of the drying oven

The temperature uniformity metric was determined by establishing a spatial average reference temperature and calculating the maximum absolute deviation from this benchmark. Figure 11 confirms compliance with blast drying oven standards, demonstrating uniformity within ±2.5% of setpoint temperature (*T*). The observed bottom-to-top thermal gradient resulted from upward convective flow that generated recirculation zones with outlet heat dissipation. The gradient caused systematically lower base temperatures. This thermal behavior was most pronounced at 70 °C, where the bottom zone averaged 2.1°C below central measurement points.

Test Materials and Test Environment

The experimental rice was short-grain Hongfa 17 japonica rice and long-grain Longqing 12, harvested from Friendship Farm in Shuangyashan City, Heilongjiang Province and Jiangbei, Jiamusi. The initial moisture content of the wet base was 12.2 to 12.9%. According to the requirements of the drying test, the moisture content of the wet base was artificially adjusted to 24± 0.2% (Wang *et al.* 2021; Wang *et al.* 2022). Drying trials were conducted under controlled laboratory conditions: Hongfa17 at 12 to 17 °C and 25 to 38% RH and Longqing 12 at 28 to 32 °C and 58 to 63% RH.

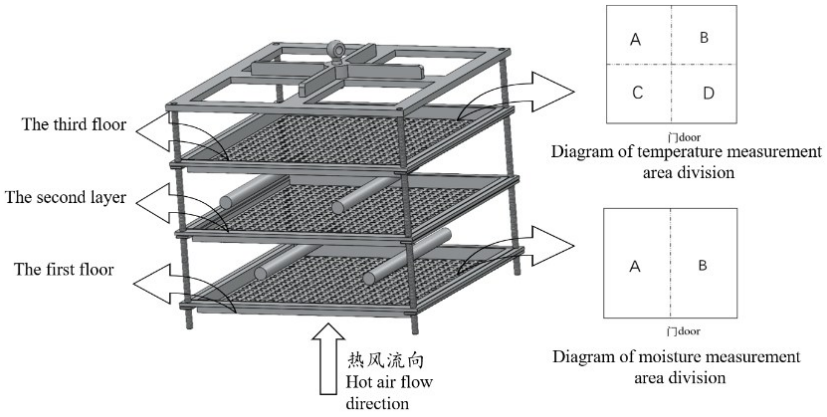

Fig. 12. Schematic diagram of drying zone test points division

To evaluate the drying performance of the test bench, this test adopted multiple varieties of rice for hot air drying tests and infrared hot air combined drying tests, respectively. Before the experiment began, 1.5 kg of rice was weighed from the processed rice samples and spread evenly in the sieve tray. The thickness was measured at multiple points to ensure uniform distribution. The parameters for hot air drying of rice were set: the hot air temperature was 45℃, the wind speed was 3 m/s, and the thickness of the thin layer of rice was 20 mm. The parameters for the infrared hot air combined drying of rice were set as follows: the hot air temperature was 45 ℃, the wind speed was 3 m/s, the thin layer thickness of rice was 20 mm, the power of the infrared radiation tube was 1000 W, and the distance from the grain layer was 300 mm. Each group of experiments was repeated three times. The mean values of the three experiments were calculated using Origin2018 software and then graphed for analysis.

The measurement of key parameters was carried out using calibrated instruments, and their inherent accuracy was taken into account to assess uncertainty: the hot air temperature was monitored by a K-type thermocouple with an accuracy of ±0.5 °C. The wind speed was measured by the Testo 405-V1 thermal anemometer with an accuracy of ±0.3 m/s. The moisture content of rice was determined by the JC-LS-01S series halogen moisture meter (Qingdao Juchuang Environmental Protection Equipment Co., LTD.), with a repeatability accuracy of ±0.05%. As shown in Fig. 10, the area of each layer of the material tray was divided into two parts (A and B) to measure the moisture content. For the materials in different areas, 20 g of rice was randomly selected every 20 minutes, and the moisture content was measured three times. The average value was taken as the measured value. To measure the temperature at the center positions of the four zones (A, B, C, and D) (Fig. 10), the temperature values at the material center positions in different zones were recorded every 10 minutes.

Determination of Test Indicators

The W_t dry base moisture content was calculated as follows,

$$W_t = \frac{M_t - G_d}{G_t} \tag{9}$$

where W_t is the dry base moisture content of rice, M_t is the mass of rice when dried, G_d is the dry matter mass of rice, and G_t is the mass of rice when dried.

The dryness uniformity across distinct zones of the material thin-layer was evaluated using Christian's Uniformity Index (CU), a metric based on the statistic of mean absolute deviation (Yu*et al.* 2020). The formulation is expressed as follows,

$$C_{Um} = \left(1 - \frac{\sum_{i=1}^{j} \left| M_i - \bar{M} \right|}{g\,\bar{M}} \right) \tag{10}$$

where M_i is the moisture content of the sample material, $\bar{M}$ is the average moisture content of sample materials, g is the number of samples, and C_{Um} is the drying uniformity coefficient.

Data Processing and Analysis

All trials were conducted in triplicate independent runs, with final results reported as the mean value of three replicates with standard deviation. Moisture content and temperature data underwent statistical analysis using Microsoft Office Excel 2021. Graphical representations were generated through Origin 2018.

RESULTS AND DISCUSSION

This study systematically evaluated the uniformity of the thermal field and the uniformity of material drying in the drying oven by monitoring the drying characteristics, drying rates, and grain layer temperature distribution of different varieties of rice. According to the dynamic characteristics of rice dehydration, the drying process of rice can be divided into two distinct stages. The first stage is the "heating and accelerating dehydration stage". During this stage, hot air convection serves as the primary heat transfer medium, rapidly raising the temperature of the rice grains through forced convection and effectively removing the free moisture on their surface. At this time, the removal of moisture mainly occurs on the surface of the material, and the evaporation resistance is small, thus showing a relatively high drying rate. Subsequently, the drying process transitions to the "deceleration dehydration stage". When the grain temperature stabilizes and the surface free water is almost completely evaporated, the drying rate is then subject to the migration rate of internal moisture. At this point, what needs to be removed is the bound water that is more closely bound to the material matrix, which requires higher energy and significantly increases the resistance of the path for the internal water to diffuse outward.

As can be seen from Fig. 11, the drying characteristic curves of rice under different drying processes exhibited the same changing trend: they first decline rapidly and then the slope tended to flatten. During the "heating and accelerating dehydration stage", the surface moisture of the grain grains was rapidly evaporated, and their moisture content dropped significantly. However, in the "decelerating dehydration stage", the drying and dewatering rate of rice was relatively stable. The main reason for this is that more heat is required to dry the bound water of the rice in this stage (Xu *et al.* 2016; Li *et al.* 2018; Liu *et al.* 2024). In the drying experiment of Hongfa rice seeds, the drying time of the first layer of rice was 160 minutes, which was 37.5% shorter than that of the third layer of rice, which was 220 minutes (Fig. 11a).

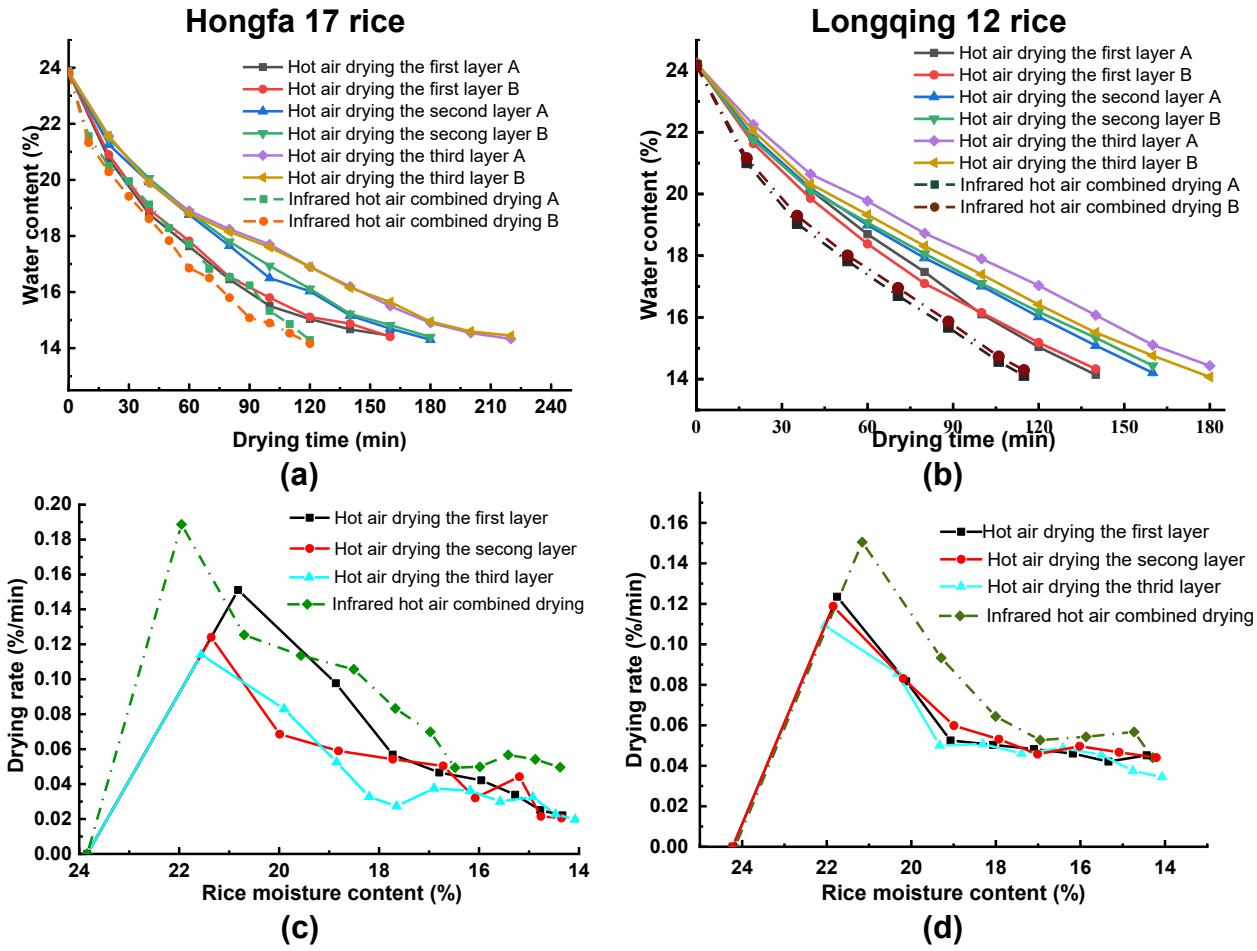

Fig. 13. Drying characteristic curves (a, b) and drying rate curves (c, d) for Hongfa 17 rice (a, c) and Longqing 12 rice (b, d)

The main reason was that the heat convection first comes into contact with the first layer of material. As a result, more heat accumulates inside the first layer of rice, and the internal temperature rises rapidly, accelerating the evaporation of free water on the surface of the rice. In addition, due to the uneven wind speed at the bends caused by thermal convection, the drying characteristic curves in different drying areas showed slight differences, but no significant differences ($P<0.05$). This is mainly reflected in the fact that the drying rate near the inner side of the curve is smaller than that near the outer side.

As shown in Figs. 13a and 13b, the combined drying time of short-grain rice with Hongfa 17 infrared hot air was 140 minutes, which was 18.8% less than the single hot air drying time of 160 minutes. For the same long-grain rice, the infrared combined hot air drying of Longqing 12 effectively shortened the drying time by 50 minutes compared with the single hot air drying. However, the uniformity of infrared hot air combined drying was lower than that of single-layer drying in single hot air drying. This is because: infrared radiation is in the form of electromagnetic waves, and the thickness of the material it can penetrate is limited, resulting in a decrease in the infrared radiation received inside the material. As a result, the moisture diffusion of the rice changes, and the uniformity of drying decreases.

It can be seen from Figs. 13c and 13d that in the stage of heating up and accelerating dehydration, having sufficient heat and wind speed can meet a relatively fast drying rate. At this point, the advantage of infrared heating is not obvious. The heat absorbed by the rice is mainly used to evaporate the free water on its surface. When the moisture content of rice is lower than 16.5% (during the deceleration dehydration stage), the removal of bound water requires overcoming a higher energy barrier, and the drying rate is restricted by the internal moisture diffusion. At this point, the advantages of infrared radiation technology are highlighted. Its energy penetrates the grains in the form of electromagnetic waves, directly stimulating the movement of water molecules to generate internal heat. This not only establishes a driving force for water diffusion from the inside out (consistent with the diffusion direction), but it also reduces the temperature gradient within the grains, thereby effectively lowering the resistance to water diffusion. This mechanism is consistent with the findings of Zhang *et al.* (2015) and Xie *et al.* (2021) in the drying of porous materials. This study further reveals that under the condition of uniform airflow distribution (optimized in this paper), the synergistic effect of infrared hot air combined drying at this stage is particularly significant, and the drying rate is significantly improved compared with single hot air drying (Figs. 11c, d). This is consistent with the infrared-assisted advantage rule observed by Jeevarathinam *et al.* (2025) in other agricultural products. The present findings have confirmed the universal value of this technology in improving the drying efficiency of heat-sensitive grains in the later stage.

As can be seen from Figs. 14a and 14c, when drying with hot air alone, the material temperature rose rapidly in the early stage, rose slowly in the later stage, and then gradually stabilized. In the macro heating air drying experiment: when the third layer of rice reached the target temperature set value, the maximum temperature difference between each thin layer of rice reached 4.7 ℃. All the temperature measurement points of the lower layer of rice after its temperature stabilized were at 42±0.5 ℃, while the average temperature of the third layer was lower. The reason for this is that the hot air consumed a large amount of heat and carried water vapor when passing through the first and second layers, and the flow rate was relatively high near the exhaust port, causing the surface heat of the third layer of rice to be lost to the air.

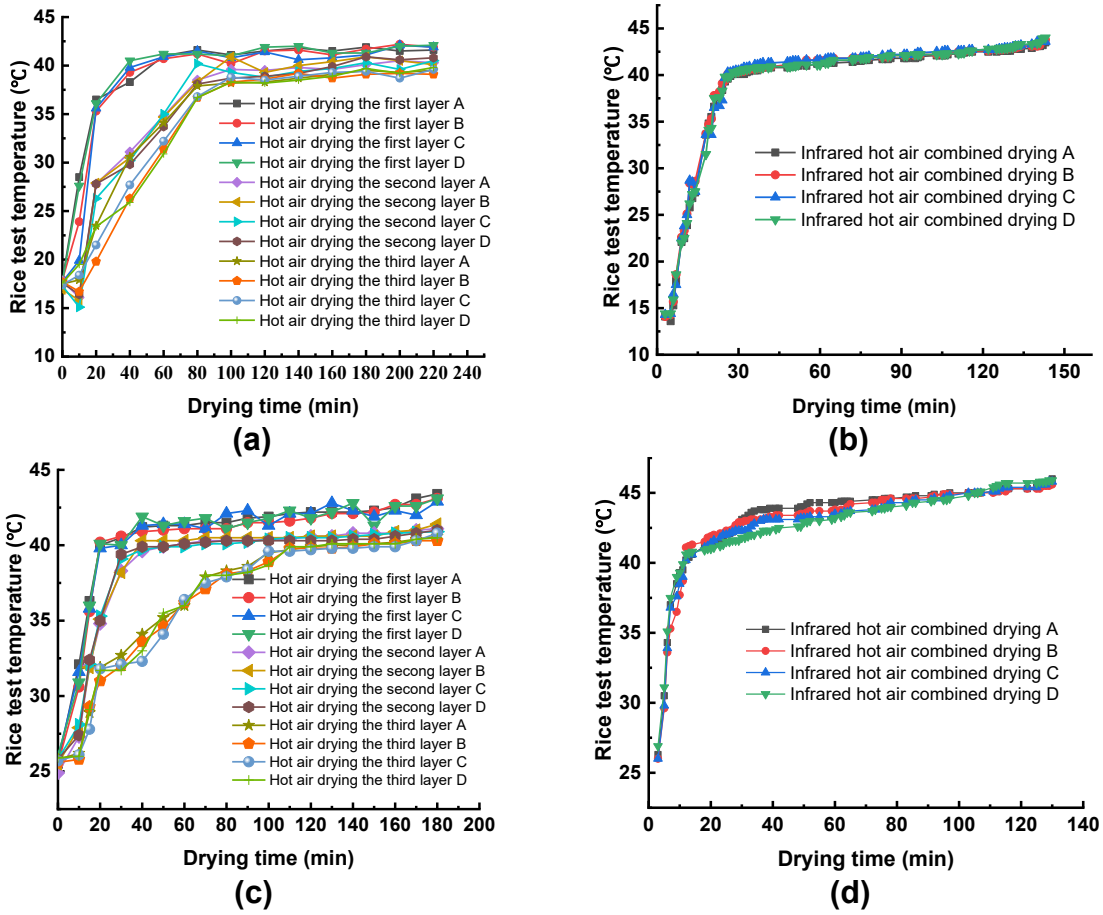

Fig. 14. Temperature profiles for materials in different drying zones. (a) Hongfa 17 rice with hot air drying, (b) Hongfa 17 rice with infrared combined with hot air drying, (c) Longqing12 rice with hot air drying, and (d) Longqing12 rice with infrared combined with hot air drying

It can be seen from Figs. 14b and 14d that the time for the infrared hot air combined drying of short-grain Hongfa 17 japonica rice to reach the target temperature set value was 30 minutes, which was 45% less than that of the hot air drying alone. The maximum temperature difference between each area of the thin layer of rice reached 2.8 °C. The maximum temperature difference of the infrared hot air combined drying of the long-grain Longqing 12 reached 2.9 °C, and the time to reach the target temperature set value was about 25 minutes.

In summary, the drying uniformity coefficients of Hongfa 17, which combined hot air drying and infrared hot air drying, were 85.37% and 85.9% respectively, while those of Longqing 12, which combined hot air drying and infrared hot air drying, were 84.59% and 84.50% respectively. The results show that the test bench met the requirements of drying uniformity under different rice drying processes.

CONCLUSIONS

1. This paper describes the designing and implementation of an infrared hot air combined drying test bench. By optimizing the airflow distribution in the upstream pipeline, the aim was to solve the problems of heating and drying uniformity of materials in the drying chamber. The pipeline structure was optimized by gradually reducing the diameter of the pipeline, and the optimization parameters were determined: the diameter reduction ratio was 1.5 and the diameter reduction length was 200 mm. The uniformity index and relative standard deviation of the wind speed at the outlet section of the optimized pipeline were optimized from 0.9227 and 0.2234 to 0.9723 and 0.1462. The test of pipeline unevenness showed that the relative error of the average speed between the optimized measured value and the simulated value was 1.50%, the relative error of the speed uniformity index was 6.23%, and the relative error of the speed relative standard deviation was 7.4%. It has been verified that this model can simulate the distribution of air flow quite well. The temperature uniformity test in the drying chamber showed that the temperature variation in the device's drying chamber was within ± 2.5%. The verification of wind temperature and wind speed tests showed that the measured data was close to the trend of the simulation data. After optimization, the wind speed non-uniformity coefficient of the pipe section with a diameter reduction ratio of 1.5 and a diameter reduction length of 200 mm was 0.1694, and the temperature uniformity change in the drying chamber of the device was within ± 2.5%.
2. Rice drying is a phased process, and the dominant heat sources and the main controlling factors of precipitation rates vary at different stages. During the temperature-accelerated dehydration stage, the drying rate is mainly dominated by the external heat and mass transfer efficiency. Hot air is the main influencing factor at this stage, undertaking the main role of raising the material temperature and removing surface moisture. At this stage, infrared radiation, as an auxiliary heat source, does not have a significant advantage. When the drying enters the deceleration and dehydration stage, the drying rate is dominated by the internal moisture diffusion rate. At this time, infrared radiation, with its unique bulk heating capacity, becomes the core influencing factor to overcome the internal diffusion resistance and improve the drying efficiency. The hot air takes on an auxiliary role, mainly responsible for promptly removing the water vapor that migrates from the inside to the surface.
3. The performance tests of 20 mm three-layer thick rice hot air drying and single-layer 20 mm rice infrared hot air combined drying showed that: The uneven heat distribution in hot air drying leads to significant differences in the drying rates of each layer, but the overall drying uniformity met the requirements of the hot air drying test. The temperature curves of each area in the infrared hot air combined drying and the drying characteristic curves of the materials showed relatively consistent trend changes, basically meeting the uniformity requirements of the infrared hot air combined drying equipment.

ACKNOWLEDGMENTS

This research was jointly guided by the Natural Science Foundation of Heilongjiang Province (LH2023C059).

REFERENCES CITED

Chen, K. J., Wang, S., Yan, J. C., Li, X. L., Zhang, M. Y., Zhou, T., Liu, H. F., Sun, Q., Wu, L. J., and Zhao, P. (2024). "Drying characteristics and quality of paddy under different low temperature and far-infrared drying conditions of graphene," *Transactions of the Chinese Society for Agricultural Machinery* 55(04), 346-351+384. https://doi.org/10.6041/j.issn.1000-1298.2024.04.034

Chen, P., Xu, C. C., Ji, L., Ma, Y. H., Wang, H. J., Gao, F. T., Liu, R. B., Zhou, W. X., Li, T. Q., and Zhang, Y. X. (2025). "Analysis of China's rice industry in 2024 and outlook for 2025," *China Rice* 31(02), 1-5. https://doi.org/10.3969/j.issn.1006-8082.2025.02.001

Cui, Z. T., and Zhou, L. Y. (2015). "Numerical simulation and comparative analysis of flow fields in converging nozzles and straight short tubes," *Shandong Ind. Technol.* 13, 15-16. https://doi.org/10.16640/j.cnki.37-1222/t.2015.13.002

Dai, J. W., Xiao, H. W., Bai, J. W., Zhang, W., Li, M. Q., Chen, S. P., Wang, X. L., Liu, S. X., Sun, P. F., and Hu, Z. Y. (2013). "Numerical simulation and optimum design on airflow distribution chamber of air-impingement jet dryer," *Transactions of the Chinese Society of Agricultural Engineering* 29(03), 69-76+295. https://doi.org/10.3969/J.ISSN.1002-6819.2013.03.010

Dai, J. W., Zhou, H. B., Huang, J., Li, M. Q., Chen, S. P., Zhang, W. T., Sun, L. J., Gao, X. H., Wang, C. G., and Liu, H. Y. (2024). "Effects of different drying technologies on the drying characteristics and quality of *Dictyophora rubrovolvata*," *Transactions of the Chinese Society of Agricultural Engineering* 40(06), 90-100. https://doi.org/10.11975/j.issn.1002-6819.202310096

Dong, L., Wang, S., Ouyang R., Zeng, G., Tan, G., and He, G. (2023). "Flow field simulation and structural optimization of mesh-belt pepper drying machine," *Transactions of the Chinese Society for Agricultural Machinery* 54(S1), 373-380. https://doi.org/10.6041/j.issn.1000-1298.2023.S1.040

Fan, M. L. (2020). *Resistance Reduction Optimization of Tapered and Expanded Pipe Sections in Ventilation and Air Conditioning System*, Master's Thesis, Xi'an University of Architecture and Technology, Xi'an, China.

GB/T 30435 (2013). *Electric Drying Ovens and Electric Blast Drying Ovens*, China Standards Press, Beijing.

GB/T 50243 (2016). "Code for acceptance of construction quality of ventilation and air conditioning engineering," China Standards Press, Beijing.

Geng, Z. H., Li, M. Q., Zhu, L. C., Yu, X., 3, Hu, B., Zhang, Q., Wang, J., and Yang, X. (2024). "Drying uniformity and technology of sea buckthorn with infrared combined hot air *via* temperature and humidity control," *Transactions of the Chinese Society of Agricultural Engineering* 40(06), 120-133. https://doi.org/10.11975/j.issn.1002-6819.202306120

Hu, Q. G. (2006). *Study on Drying Process of Edamame by Hot-Air and Vacuum Microwave Combination*, Master's Thesis, Jiangnan University, Wuxi, China.

Jeevarathinam, G., Pandiselvam, R., Pandiarajan, T., Deepa, J., Dinesh Kumar, S., Preetha, P., Krishnakumar, T., Asha Monicka, A., Balakrishnan, M., and Amirtham, D. (2025). "Infrared-assisted hot air drying of turmeric slices: Effects on drying kinetics, quality, efficiency, energy considerations, and mathematical modeling," *Heat Transfer* 54(3), 1965-2000. https://doi.org/10.1002/htj.23261

Jiang, D. L., Wu, M., Wang, S. Y., Wang, W., and Zheng, Z. (2022). "Design and

performance verification of infrared combined hot air drying device," *Transactions of the Chinese Society for Agricultural Machinery* 53(12), 411-420. https://doi.org/10.6041/j.jssn.1000-1298.2022.12.040

Ju, H.-Y., Zhao, S.-H., Mujumdar, A. S., Zhao, H.-Y., Duan, X., Zheng, Z.-A., Gao, Z.-J., and Xiao, H.-W. (2020). "Step-down relative humidity convective air drying strategy to enhance drying kinetics, efficiency, and quality of American ginseng root," *Drying Technology* 38(7), 903-916. https://doi.org/10.1080/07373937.2019.1597373

Li, C, Y. (2018). "Theoretical analysis of exergy transfer and conversion in grain drying process," *Transactions of the Chinese Society of Agricultural Engineering* 34(19), 1-8. https://doi.org/10.11975/j.issn.1002-6819.2018.19.001

Li, H. L., Wang, C., Hu J., Yu, H., Li, Q., and Zhang, X. (2018). "Simulation and optimum design on airflow distribution chamber of pneumatic forming machine for rice seeding-growing tray," *Transactions of the Chinese Society for Agricultural Machinery* 49(04), 94-101. https://doi.org/10.6041/j.issn.1000-1298.2018.04.011

Li, T., Jin, S, P., Huang, S, Y., and Liu, W. (2013). "Evaluation indices of flow velocity distribution uniformity: Comparison and application," *Thermal Power Generation* 42(11), 60-63+92. https://doi.org/10.3969/j.issn.1002-3364.2013.11.060

Liu, C. S. (2014). *The Mechanism and Experimental Study on Far-Infrared Radiation and Convection Method for Grain Drying*, Jilin University, Changchun, China.

Liu, C. S., Chen, S., Chen, S. Y., Iu, H. Y., Wang, S. M., Ma, L. X., Li, J. Q., Li, M. Y., and Wang, C. G. (2024). "Analysis and model exploration of paddy hot Air drying process," *Transactions of the Chinese Society for Agricultural Machinery* 55(S1), 364-372. https://doi.org/10.6041/j.issn.1000-1298.2024.S1.039

Liu, C. S., Xiao, S, W., Chen, S, Y., Zhang. Y., Wang, A. R., and Gao, X. W. (2024). "Experimental study on the effect of rice drying process on dry characteristics," *Journal of Agricultural Mechanization Research* 46(06), 175-179+184. https://doi.org/10.13427/j.cnki.njyi.2024.06.029

Liu, G, G., Luan, Z, H. (2005). "Effects of the transitional moulding surface of reducing pipe on flow rate based on finite element," *Coal Mine Machinery* 11, 69-71. https://doi.org/10.13436/j.mkjx.2005.11.029

Nuthong, P., Achariyaviriya, A., Namsanguan, K., and Achariyaviriya, S. (2010). "Kinetics and modeling of whole longan with combined infrared and hot air," *Journal of Food Engineering* 102(3), 233-239. https://doi.org/10.1016/j.jfoodeng.2010.08.024

Tao, H. G., Chen ,H. X., Xie, J. L., Shu, Z. H., Hu, Y. Y., and Lu, H. L. (2010). "Flow uniformity index based on area-weighted and mass-weighted average velocity," *CIESC Journal* 61(S2), 116-120.

Wang D. Y., Wang, J., Qiu, S., Zhan, T. Y., Tao, D. B., and Zhang, B. H. (2021). "Optimization and experimental study of tempering process parameters during hot airdrying of paddy rice," *Transactions of the Chinese Society of Agricultural Engineering* 37(17), 285-292. https://doi.org/10.11975/j.issn.1002-6819.2021.17.033

Wang, J., Wang, W. Y., Tao, D. B., Zhan, T. Y., Ji, D. P., Hao, J. M., and Wang, D. Y. (2022). "Effect of variable temperature on drying characteristics and quality of paddy rice," *Journal of Shenyang Agricultural University* 53(2), 239-247. https://doi.org/10.3969/j.issn.1000-1700.2022.02.013

Wang, X., Hu, Q., Xiao, B., and Yang, D. (2013). "Modeling simulation of combined convective and infrared radiation in rice drying process," *Transactions of the Chinese Society of Agricultural Machinery* 44(09), 145-151.

https://doi.org/10.6041/j.issn.1000-1298.2013.09.026

Wang, Y. K., Wu, C. S., Hua, C., Zhu, W, X., Chen, P, X., Xing, Y, J., Zhao, S, Y., Zhang, T, T., and Ma, J. F. (2025). "Infrared drying kinetics and water migration characteristics of peanut pods," *Chinese Journal of Oil Crop Sciences* 2025, 1-11. https://doi.org/10.19802/j.issn.1007-9084.2024240

Wu, M., Duan, H., Wang, Z. W., Li, Y., Zheng, Z. A., and Duan, Q. (2020). "Design and experiment of infrared-hot air combined dryer based on temperature and humidity control," *Transactions of the Chinese Society for Agricultural Machinery* 51(S1), 483-492. https://doi.org/10.6041/j. issn.1000-1298.2020. S1.057

Xie, Y, K., Li, X, Y., Zhang, Y., Zheng, Z., Huang, A., Qi, L., Liu, D. H., Xiao, H. W., and Liu, Y. H. (2021). "Effects of high-humidity hot air impingement steaming on *Gastrodia elata*: Steaming degree, weight loss, texture, drying kinetics, microstructure and active components," *Food and Bioproducts Processing* 127, 255-265. https://doi.org/10.1016/j.fbp.2021.03.005

Xu, F, Y., Huang, M, S., Chen, Z., and Li, C. Y. (2016). "Moisture diffusion characteristics and quality characteristics of rice during drying," *Transactions of the Chinese Society of Agricultural Engineering* 32(15), 261-267. https://doi.org/10.11975/j.issn.1002-6819.2016.15.036

Xue, H. L., and Yan, Y. T. (2023). "Kinetics and mass transfer characteristics of combined infrared-hot air drying of *Zanthoxylum bungeanum* maxim," *Journal of Agricultural Mechanization Research* 45(09), 209-216+225. https://doi.org/10.13427/j.cnki.njyi.2023.09.009

Zhang, W. P., Xiao, H. W., Gao, Z. J., Zheng, Z. A., Ju, H. Y., Liang, S., and Zheng, X. (2015). "Infrared drying properties and drying experiment of carbon fiber for agricultural production," *Transactions of the Chinese Society of Agricultural Engineering* 31(19), 285-293. https://doi.org/10.11975/j.issn.1002-6819.2015.19.039

Zhang, J. K., Zheng, X., Xiao, H. W., Shan, C. H., Li, Y. C., and Yang, T. Q. (2024). "Simulation of heat and mass transfer shrinkage and quality of yam slices dried using infrared combined hot air," *Transactions of the Chinese Society of Agricultural Engineering* 40(06), 134-145. https://doi.org/10.11975/j.issn.1002-6819.202308074

Zhang, X. G., Yao, X. D., Huang, Y., Zheng, X., Wang, Q., Wei, S. Y., Cao, Y. X., and Zhu, R,G. (2019). "Design and test of disc combined dryer with hot wind and infrared," *Journal of Agricultural Mechanization Research* 41(01), 253-257. https://doi.org/10.13427/j.cnki.njyi.2019.01.047

Article submitted: July 26, 2025; Peer review completed: November 22, 2025; Revised version received and accepted: December 4, 2025; Published: January 28, 2026.
DOI: 10.15376/biores.21.1.2330-2350